Ceramics International 48 (2022) 15877–15888

Contents lists available at ScienceDirect

Ceramics International

journal homepage: www.elsevier.com/locate/ceramint

Unravelling the origin of the capacitance in nanostructured nitrogen-doped carbon - NiO hybrid electrodes deposited with laser

Pablo García Lebière [a], Enikö György [a,b], Constantin Logofatu [c], Denys Naumenko [d], Heinz Amenitsch [d], Piu Rajak [e], Regina Ciancio [e], Ángel Pérez del Pino [a,*]

[a] Institute of Materials Science of Barcelona, ICMAB-CSIC, Campus UAB, 08193, Bellaterra, Spain
[b] National Institute for Lasers, Plasma and Radiation Physics, PO Box MG 36, 77125, Bucharest, Romania
[c] National Institute for Materials Physics, PO Box MG 7, 77125, Bucharest, Romania
[d] Institute of Inorganic Chemistry, Graz University of Technology, Stremayrgasse 9/V, 8010, Graz, Austria
[e] Istituto Officina dei Materiali-CNR, Area Science Park, S.S.14, Km 163.5, 34149, Trieste, Italy

ARTICLE INFO

Keywords:
Electrochemical capacitors
Hybrid electrode
Carbon nanostructures
MAPLE
SPECS

ABSTRACT

The full knowledge of the charge storage mechanisms occurring in complex composite electrodes is key for the straightforward development of advanced electrochemical capacitors. In this work, hybrid electrodes composed of reduced graphene oxide, multiwall carbon nanotubes and NiO nanostructures were fabricated through reactive inverse matrix assisted pulsed laser evaporation technique. Nitrogen doping of the carbon nanostructures was carried out by introducing ammonia, urea and melamine precursors in the target. The N-doped graphene electrodes exhibited a significant capacitance enhancement as compared to non-doped ones. This fact is commonly ascribed to faradaic mechanisms. However, our structural-compositional studies point to a significant change of the structural configuration of the composites at the nanoscale upon the nitrogen functionalization as the source of the electrodes' capacitance enhancement. The composites fabricated with urea precursor exhibited the highest capacitance, and this fact was associated with the presence of pyridinic N groups that triggered the formation of a high amount of structural defects (vacancies – boundaries) and microporosity, not observed in the samples synthesized with other precursors that mainly contained pyrrolic-graphitic N.

1. Introduction

Electrochemical capacitors (ECs) are appealing devices that are attracting great attention due to their ability to rapidly store and deliver electric energy, allowing high power charge and discharge processes. ECs based on electrochemical double layer (EDL) mechanism store and release the energy by means of charge separation processes at the electrochemical interface defined between the electrode and the electrolyte [1–3]. EDL electrochemical capacitors are able to store large amounts of charge as compared to conventional electrostatic capacitors, but still quite lower than rechargeable batteries. Highly porous conductive materials, as nanostructured carbons (activated carbon, graphene, carbon nanotubes), are the most promising electrode materials to be used in EDL capacitors due to their high surface area and electric conductivity, besides mechanical robustness [2,4–7].

In order to surpass the capacitance limitations of EDL capacitors based on nanostructured carbons, strategies like their combination with electroactive entities are tackled. This can be attained by either the carbon backbone functionalization with heteroatom functional groups or through their decoration with pseudocapacitive nanostructures [8–12]. It is generally accepted that the functionalizing chemical groups, as well as the structural defects caused by the substitutional heteroatoms, lead to the concentration of local charges that promote the occurrence of electrochemical charge transfer reactions. In particular, N-doping of the graphene structure has been revealed as an effective way for tuning its electrical-electrochemical properties: substitutional graphitic N induces a n-type semiconducting nature in graphene besides electron-hole asymmetric transport, improving its electric conductivity and hydrophilic properties. Additionally, pyridinic and pyrrolic N, found at the edges and defect sites of graphitic layers, prompt a p-doping effect besides electrochemical activity leading to faradaic charge storage [8,13–17]. On the other hand, pseudocapacitive nanostructures supported on the carbon structure undergo fast surface redox reactions leading to a significant contribution to the charge storage, much higher

* Corresponding author.
E-mail address: aperez@icmab.es (Á. Pérez del Pino).

https://doi.org/10.1016/j.ceramint.2022.02.128
Received 16 November 2021; Received in revised form 7 February 2022; Accepted 12 February 2022
Available online 18 February 2022

than EDL mechanisms occurring on the carbon surface. Accordingly, the carbon material would act as a porous and conductive scaffold allowing the access of the electrolyte ions and the fast transport of the charges to the current collector. Therefore, the use of hybrid electrodes combining (doped) carbon and pseudocapacitive nanostructures represents a promising approach for the manufacture of both symmetric and asymmetric ECs with highly improved capacitance [1,3,18–20].

Not only advanced composites must be synthesized for attaining electrodes with higher electrochemical performance, but also innovative approaches shall be developed for overcoming the limitations of the conventional manufacturing methods. It is worth noticing that reactive inverse matrix assisted pulsed laser evaporation (RIMAPLE) technique has exhibited high versatility for obtaining carbon-based hybrid electrodes by simultaneous deposition and photo-induced chemical reactivity of the irradiated precursor materials [21–26]. In particular, RIMAPLE experiments carried out by pulsed UV laser irradiation of frozen aqueous dispersions containing graphene oxide (GO) sheets, multiwall carbon nanotubes (MWCNTs), NiO nanoparticles (NPs), and nitrogen containing reactive precursors allowed to deposit electroactive films composed of N-doped reduced GO (NrGO) and MWCNTs decorated with small NiO NPs [23,27]. The porous NrGO-MWCNT framework exhibited high electric conductivity, whereas NiO NPs added mechanical stability to the rGO structure as well as pseudocapacitance. Moreover, the N-doping varied in terms of the amount of nitrogen incorporation as well as the type and relative quantity of the nitrogen containing chemical groups in the graphene structure depending on the precursor molecule used. The N-doping induced an enhancement of the capacitance of the NrGO-MWCNT-NiO hybrid electrodes but this enhancement varied significantly depending on the used N-containing precursor. Remarkably, and contrarily to the generally accepted viewpoint, the obtained results suggested that an important contribution of the N-doping process to the energy storage could be originated by structural modifications beside faradaic-based reactions, and this fact has been also claimed by other authors before [28]. In this case, higher microporosity associated with doping-induced defects, not measurable by Brunauer–Emmett–Teller method, would increase the active surface in contact with the electrolyte. Furthermore, the edges linked to graphitic planes and defect sites (vacancies) could prompt convergent diffusion processes leading to orders of magnitude higher specific capacitance and electron transfer rates [29]. Therefore, the real origin of the increase of the capacitance with the N-doping remains still unclear in this type of electrodes and further investigations should be carried out.

This work aims to provide key elements for elucidating the main origin of the capacitance increase of the rGO-MWCNT-NiO hybrid electrodes upon N-doping of the nanocarbon structures by using different N-containing precursors (ammonia, urea and melamine). Compositional and structural studies were carried out through X-ray photoelectron spectroscopy (XPS), high resolution electron microscopies, small angle X-ray scattering (SAXS) and Raman spectroscopy techniques. The electrochemical analysis of the electrodes was performed via step potential electrochemical spectroscopy (SPECS). The obtained results provided a clear connection between the nanostructure of the composite, which indeed is also related to the type of functionalization, and their electrochemical performance. All the samples showed the formation of pyrrolic N. However, the electrode synthesized with urea precursor, which was the one exhibiting the highest capacitance, also presented the formation of pyridinic N, the highest density of structural defects (with more vacancies-boundaries than the other rGO-MWCNT composites) and the most porous matrix.

2. Experimental

Different types of aqueous dispersions were produced by the addition to deionized water solvent of graphene oxide powder (GO, formed by up to 15 layers' thick sheets and about 0.5–1 μm lateral size; NanoInnova Technologies), multiwall carbon nanotubes doped with carboxylic groups (MWCNT, about 1 μm long and 10 nm in diameter; Sigma-Aldrich), and NiO nanoparticles (NPs, ca. 50 nm in diameter; Sigma-Aldrich). To induce the chemical reactivity and nitrogen doping of the carbon nanoentities, additional dispersions were created by adding nitrogen-containing precursors (ammonia, urea and melamine; Sigma-Aldrich). Table 1 presents the concentration of all the precursors used for the synthesis of the dispersions. These concentration values were selected after an optimization study and allowed to get homogeneous liquid dispersions with the highest possible concentration of precursors. Afterwards, the dispersions were magnetically stirred for at least 1 h and sonicated for 1 min at room temperature for avoiding the aggregation of the precursors and obtaining completely homogeneous dispersions. The MAPLE targets were prepared by filling 3 mL aluminium holders with the viscous dispersions, followed by their rapid freezing through immersion in liquid N_2. Next, the MAPLE targets were positioned inside the deposition chamber and kept frozen during the deposition process using a liquid N_2-cooled holder. The temperature at the MAPLE target, measured by an IR thermometer, was about 200 K.

The deposition of the electrodes was carried out by submitting the targets to laser pulses of 266 nm wavelength and about 5 ns duration, using a Brilliant B Nd:YAG laser system (Quantel). 6000 pulses with 0.4 J cm^{-2} laser fluence were applied to the frozen targets at a 10 Hz repetition rate. During the deposition process, the laser beam scanned continuously the target surface with an incident angle of ca. 45°. Special care was taken for avoiding the formation of deep craters in the target and to maintain the plasma plume as vertical as possible (pointing to the substrate). Flexible 1 × 1 cm^2 substrates made of 0.1 mm-thick stainless steel (grade 316L; Advent RM), were placed in front of the frozen target at a separation distance of 4 cm. The deposition process was carried out in 20 Pa N_2 background gas environment prior emptying to a residual pressure of 0.1 Pa.

Numerical simulations of the laser-induced heating of the irradiated nanostructures submitted to one laser pulse within the water ice matrix were performed with COMSOL Multiphysics 5.6 software. The coupling of the optical and thermal response of GO sheets, MWCNTs, and NiO NPs were calculated by solving the heat equation in 3D models using the finite element method. Only photothermal processes were considered. The initial temperature was set to 200 K, and the geometry of the simulated nanoentities was simplified to parallelepipeds with a size of 500 × 500 × 1–2 nm^3, 10 × 10 × 1000 nm^3, and 50 × 50 × 50 nm^3 for (single- and double-layer) GO sheets, MWCNT and NiO NP, respectively. The used optical and thermodynamic magnitudes of the simulated materials were gathered from various references (Table S1, Supporting Information) [21,30–33].

The characterization of the obtained electrodes' morphology was performed through extreme high resolution scanning electron microscopy (XHRSEM) by means of a Magellan 400L system (FEI). The structural features at the nanoscale were investigated by means of high resolution transmission electron microscopy (HRTEM) and selective area electron diffraction (SAED) using a JEOL 2010 UHR field emission gun microscope operated at 200 kV with a measured spherical aberration coefficient of 0.47 ± 0.01. Additional measurements were carried out on Si substrates through grazing-incidence small-angle X-ray scattering (GISAXS) at the Austrian SAXS beamline at Elettra synchrotron facility (Trieste, Italy) at photon energy of 8 keV [34]. The beam size was

Table 1
Labels used for the description of the synthesized targets and their corresponding composition.

Target	Composition
(5/0/5)	5 wt% GO, 5 wt% NiO
(5/1/5)	5 wt% GO, 1 wt% MWCNT, 5 wt% NiO
(5/1/5)A	5 wt% GO, 1 wt% MWCNT, 5 wt% NiO, 2 M ammonia
(5/1/5)U	5 wt% GO, 1 wt% MWCNT, 5 wt% NiO, 2 M urea
(5/1/5)M	5 wt% GO, 1 wt% MWCNT, 5 wt% NiO, 0.3 M melamine

set to 1.5 × 0.2 mm^2 (HxV). The sample to detector (Pilatus3 1 M, Dectris) distance was adjusted to 711 mm calibrated with silver behenate as a reference pattern. The measurements were initially performed with 60 s exposure time at 15% humidity. The incident angle was set to 0.2°, i.e. below critical angle of Si substrate in order to satisfy surface sensitive conditions. The experimentally recorded 2D patterns were transformed into 1D I(q) patterns by means of horizontal (in-plane) cuts at the position of the Yoneda wing using SAXSDOG software [35]. The successive data correction for the fluctuations of the primary intensity, fitting of the data, and evaluation of correlation length were performed using IGOR Pro (IGOR Pro 7.0.8.1, WaveMetrics). For further study of the composite structures, in particular the accessibility of pore structures, GISAXS measurements were also performed in controlled relative humidity environment. These experiments were carried out by recording scattering patterns continuously (every 30 s with 10 s exposure time) during 200 min while applying increasing-decreasing humidity ramps in the 15–90% range. Moreover, the chemical composition of the electrodes was also analysed through X-ray photoelectron and micro-Raman spectroscopies. XPS measurements were done in ultra-high vacuum (~10^{-7} Pa) with a SPECS spectrometer based on a Phoibos 150 electron energy analyser working in constant energy mode. An aluminium anode (Al Kα 1486.74 eV) was used as monochromatic X-ray source. Wide range spectra were acquired over 1400 eV binding energies using a 50 eV analyser pass energy, and high resolution spectra were also recorded over 20 eV ranges at 10 eV pass energy with an energy resolution of 0.7 eV. The C1s signal of adventitious carbon (284.8 eV) was employed as reference for the calibration of the binding energies for all spectra. The Raman spectroscopy measurements were carried out in air with a home-built optical set-up consisting of 532 nm DPSS laser with 2 MHz linewidth (Cobolt - Samba), which is focused on the sample through a microscope objective (Olympus MPLFLN-BD, x50, N.A. = 0.8) to a spot smaller than 1um. Spectra were acquired in backscattering configuration using a 750 mm spectrometer equipped with 600 lines per mm gratings (Shamrock SR-750), and a EM CCD (Andor Newton).

The charge storage mechanisms and kinetic diffusion of the electrodes were studied through step potential electrochemical spectroscopy (SPECS) with a Keithley 2450-EC Electrochemistry Lab equipment. The 0-0.8-0 V voltage window was scanned through voltage steps of 25 mV. After each voltage change, the evolution of the current with time was acquired during 60 s with a 10 ms sampling interval. The deposited films were used as working electrodes in a three-electrode electrochemical cell (Bio-Logic). The measurements were performed using an Ag/AgCl reference electrode (3 M KCl internal solution) and a Pt wire counter electrode in a 1 M Na_2SO_4 aqueous solution.

3. Results and discussion

As already described above, the frozen targets submitted to laser irradiation are composed of aqueous dispersions of GO sheets, MWCNTs, NiO NPs, and N-containing precursors. The matrix, composed of water ice and dissolved N-containing molecules practically does not absorb the UV laser radiation [36–39]. Therefore, most of the photons are absorbed in the GO sheets, MWCNTs and NiO NPs leading to mainly photothermal mechanisms that induce their fast heating [21,26,33]. The thermal simulation of the irradiated nanoentities was carried out through 3D simple models (parallelepipeds with the proper dimensions). As observed in Fig. 1a, the GO monolayers of about 500 nm of lateral size and 1 nm in thickness would barely attain 220–230 K, which is about the considered water ice sublimation temperature at 20 Pa pressure [30]. However, the 2 nm-thick double-layer GO sheets increase their maximum temperature values, reaching up to ca. 290 K in just 6 ns. Accordingly, thicker multi-layered GO plates are expected to develop higher temperatures beyond the water ice sublimation point. As a result, it could be hypothesized that the thickest GO flakes would undergo both thermally- and photochemically-activated reduction reactions, whereas

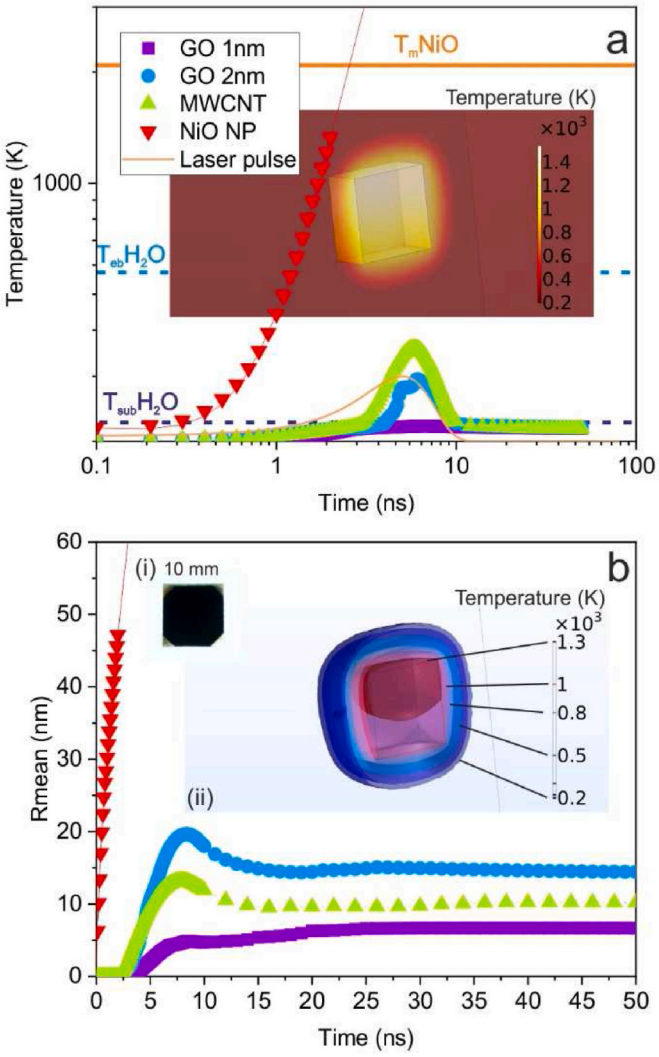

Fig. 1. (a) Simulated temperature evolution with time at the surface of GO sheets (1 and 2 nm thick), MWCNT, and NiO NP during one laser pulse irradiation. Inset: temperature distribution at the NiO NP at 2 ns. The sublimation and explosive boiling temperatures of water ice are also indicated. (b) Evolution of the vaporized water mean radius with time. Inset: (i) photograph of a deposited electrode, (ii) temperature isosurfaces in NiO NP and the surrounding matrix.

thermal effects in the thinnest GO sheets would be negligible for reduction [40,41]. In this last case, photolytic mechanisms would be mainly responsible of the GO reduction. In a similar fashion, the simulated temperature attained in the MWCNT surface reaches ca. 360 K at 6 ns from the beginning of the laser pulse, probably also causing a loss of part of their carboxylic functionalization [42]. In all these cases, sublimation of the ice surrounding these nanoentities is expected. Conversely, the NiO NPs experience a very rapid heating, even reaching the spinodal temperature of water (about 90% of the critical temperature; 575 K) in just 1.2 ns, provoking the explosive boiling of the adjacent water ice [30]. Furthermore, the NPs would reach the melting temperature of NiO (ca. 2200 K) at just 2.6 ns, probably undergoing hydrodynamic phenomena like dewetting and coalescence. It has to be noted that the model considered the incident laser fluence at the target (0.4 J cm^{-2}), though partial absorption and scattering effects would diminish the fluence reaching the nanostructures located in the inner part of the MAPLE target, leading to lower temperatures.

The inset of Fig. 1b shows the temperature isosurfaces in NiO NP simulation, revealing that the largest temperatures are developed inside

the NP, as well as a high temperature gradient in the matrix around the NP (ca. 2×10^{10} K/m). In order to estimate the quantity of frozen matrix transformed to gas, the volume of the matrix surrounding the studied nanoentities with a temperature above its sublimation temperature (220 K) was recorded as a function of time and, from this volume, the average radius of vaporized water was calculated (Fig. 1b). This volume/average distance also delimits the spatial range in which the N-containing molecules could be thermally activated and interact with the nanoentities, leading to N-doping. Consequently, these chemical reactions occurring in the gaseous volume around the nanoentities would take place at the initial stages of the deposition process. As observed, the maximum value of the mean radius of sublimated matrix around the monolayer and bi-layer GO, besides the MWCNT is small, about 6 nm, 20 nm, and 13 nm, respectively. Conversely, the mean radius of vaporized water around the NiO NPs linearly increases with time in a steep fashion, achieving ca. 56 nm at the time in which the NiO NP reaches its melting temperature. Accordingly, a significantly larger volume of matrix changes to the gas phase around the NPs as compared to the carbon nanostructures. Furthermore, higher temperatures developed around NiO NPs would also increase the doping molecules reactivity. This effect would be increased in aggregated NPs or if various molten NPs droplets join during the irradiation process. Additionally, the matrix surrounding the NPs experiences explosive boiling, which is more energetic than sublimation and, hence, develops higher gas pressure. As a consequence, the micro-explosion of the gas bubble created around the nanoentities thrusts them and drives their deposition onto the facing substrate, coming the larger contribution from the NPs. This fact would explain the higher rate of deposition of GO-based films when NiO NPs are included in the MAPLE target [21]. The overall result of all the described processes is the deposition of a homogeneous black film, about 1–2 μm thick, after the accumulation of 6000 laser pulses (Fig. 1b inset). The films are adherent to the substrate, mechanically robust even after mild bending, and show a rough aspect.

The surface morphology and nanostructure of the electrodes were studied with SEM and TEM. Fig. 2a shows a XHRSEM image of the (5/1/5)U sample surface which is representative of all the (5/1/5) electrodes. The morphology of the material reveals a rough and heterogeneous mixture of rGO sheets, from hundreds of nm to ca. 1 μm in lateral size, and carbon nanotubes, up to ca. 1 μm in length. The rGO flakes display crumpled shapes and irregular edges, forming aggregates and cavities of about tens to hundreds of nm between the flakes/aggregates. Bent MWCNTs appear randomly distributed over the rGO sheets, as well as in form of intertwined beams of nanotubes. Additionally, higher magnification images reveal that the rGO and MWCNT surfaces are coated with nm particulates and aggregates with up to a few tens of nm in size, associated to NiO (Fig. S1, Supporting Information). It is worth recalling that the initial size of NiO NPs is about 50 nm. Therefore, the presence of stuck NPs with significantly smaller and larger sizes would point out to the development of dewetting and coalescence mechanisms of the molten material before resolidification, as anticipated by the thermal simulations (Fig. 1a). The sample (5/0/5), with no presence of MWCNTs, shows a more compact morphology composed of rGO sheets decorated with NPs.

Further, TEM analyses were used to get more insights into the structural morphology of different deposited materials. The TEM image of the GO raw material (presented in Fig. S2a) shows the presence of few stacked layers. The structure of GO sheets displays a continuous conformation with straight wrinkles and without nanoholes. The SAED and HRTEM image analyses (shown in Figs. S2b and 2c, respectively) disclose the crystalline nature of GO with measured interplanar distances of 0.15, and 0.24, 0.28 nm which correspond to strained (110) and (100) crystallographic planes of GO, respectively [43]. The TEM analyses of the raw MWCNTs reveal a well-defined structure of MWCNT with about 15 concentric layers and without any significant structural defects (Figs. S3a and b). The graphitic crystallographic structure of MWCNT is confirmed from electron diffraction. The SAED pattern presented in Fig. S3c shows reflections compatible with an interplanar distance of 0.34 nm corresponding to (002) planes. In contrast, the deposited materials show remarkably different features. First of all, the samples show the presence of NiO NPs with size ranging from 1 nm to 10 nm fully covering the carbon nanostructures. Electron energy loss spectroscopy compositional maps of C, N, O, and Ni elements were obtained (Fig. S4), confirming the presence of Ni in the NPs that totally cover the MWCNT and rGO surface. The small NPs are much more numerous than the large ones, and no noteworthy differences in the NP distribution were visible between the samples. The rGO sheets appear more crumpled than the raw GO ones, with rag-shaped morphology and some degree of amorphization, probably induced by the crystalline

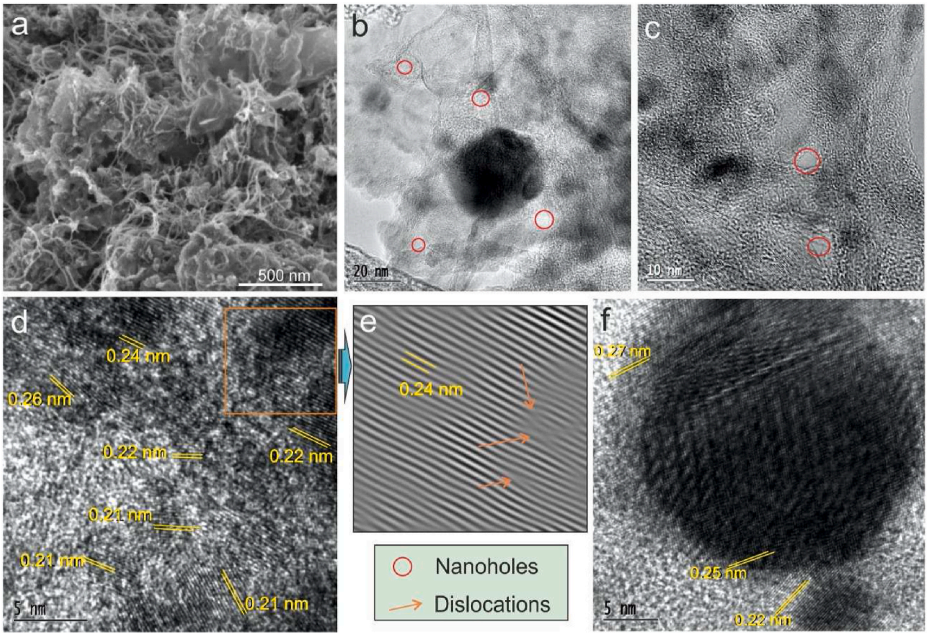

Fig. 2. (a) XHRSEM image of (5/1/5)U sample. TEM images of (b) (5/1/5)M and (c) (5/1/5)A emphasising nanometre-sized holes. HRTEM images of (d) (5/1/5)M and (e) selected area filtered through FFT showing atomic planes of (111) NiO, and (f) detail of a twinned NiO NP in (5/1/5)A.

defects created after the high temperature exposure and reduction process during the laser irradiation. The graphitic structure of the MWCNTs also shows some amorphization and discontinuity at the external layers for the same reasons. Remarkably, the rGO flakes of all the samples except (5/0/5) and (5/1/5) exhibit the presence of few to 10 nm-sized holes (Fig. 2b and c). Hence, it could be pointed out that the origin of such holes would be the laser-induced chemical reaction of the GO material with the N-containing molecules contained in the matrix. The HRTEM images also depict that the NiO NPs are highly crystalline with measured interplanar distances of 0.15–0.18 nm, 0.21–0.22 nm, and 0.24–0.25 nm corresponding to the (220), (200), and (111) crystallographic planes of cubic NiO (JCPDS 00-047-1049), respectively (Fig. 2d). The value and dispersion of these interplanar distances suggest the formation of highly strained structures, which would also explain the high density of edge dislocations identified in selected areas filtered by fast Fourier transform (FFT; Fig. 2e), as well as the creation of twin structures exhibited by some NPs (Fig. 2f). All these phenomena account for the extreme kinetic conditions undergone by the crystals during their growth at huge temperatures during very short times. Additionally, the (100) and (110) crystallographic planes of rGO as well as (002) of MWCNT were also recorded in the deposited samples.

As observed in EELS maps, oxygen and nitrogen elements are homogeneously distributed across the carbon nanostructures (Fig. S4). XPS characterization was used for the quantitative analysis of the carbon materials composition. Wide-scan surveys revealed the presence of C, O, N and Ni elements (Fig. S5a). The reduction and nitrogen incorporation processes in the rGO-MWCNT structures were studied through the C/O and N/(N + C) atomic ratios assessed from the XPS surveys, after subtraction of the NiO contribution from O concentration (Fig. 3a). As observed, the C/O ratio slightly increases from 2.5 in sample (5/0/5) to 2.9 in (5/1/5) that is, by incorporating the MWCNTs into the layer, suggesting that either the relative oxygen-to-carbon content of the MWCNTs is lower than that of the rGO or the reduction process is more aggressive due to the higher temperatures developed in the MWCNTs and surrounding matrix upon the laser irradiation. Besides, an increase of the C/O ratio is also observed by adding N-containing molecules, up to ca. 3.5 with the addition of ammonia and urea, and achieving 5.3 in the case of melamine. Then, it could be pointed out that the N-doping process induces greater reduction of the GO sheets and MWCNTs, besides the possible addition of carbon structures. On the other hand, the highest inclusion of nitrogen in the rGO structure is attained in (5/1/5) M (N/(N + C) ratio of 15.6), followed by the samples deposited in the presence of urea (10.9) and ammonia (6.6). The (5/1/5) and (5/0/5) samples exhibit the lowest nitrogen ratio, about 2.5–3.3, which is caused by the reactive interaction of the heated carbon nanoentities, originating from the MAPLE target towards the substrate, with the background N_2 gas filling the chamber.

The high resolution XPS analyses allow to determine the type of functional groups in the rGO and MWCNT structures. For illustration, Fig. 3b presents typical C1s and N1s spectra of the (5/1/5)U sample. The C1s spectra were deconvoluted into five components: C1 (centred at 284.7 eV), assigned to C=C sp [2] with, probably, some contribution of sp [3] C–C; C2 (at 285.6 eV), corresponding to hydroxyl groups; C3 (at 286.7 eV), assigned to epoxide functionalization; C4 (at 288.9 eV) related to carboxylic groups; and C5 (at 290.4 eV), associated to a shake-up satellite caused by a π–π* transition at graphene domains [44, 45]. In concordance with previous works [23], C1–C4 peaks appear in all the samples, whereas C5 only appears in (5/1/5)M and is very weak (Fig. S5b). In all the cases, the component associated to C=C is the most intense one, especially in (5/1/5)U. The N1s spectra were deconvoluted into four components: N1 (centred at 398.7 eV), assigned to pyridinic nitrogen; N2 (at 399.9 eV), corresponding to pyrrolic-amine-amide groups; N3 (at 401.2 eV), associated to quaternary (graphitic) nitrogen; and N4 (at 404.5 eV), attributed to pyridinic NO_x [46–48]. It is worth mentioning that a contribution of pyridinic and pyrrolic N–C bonds should be considered to the C2 and C3 peaks of the C1s spectrum [49], imposing a slight decrease of the calculated percentage of hydroxyl and epoxide groups. Remarkably, the content of nitrogen groups vary from one sample to another: all the samples exhibit the presence of pyrrolic-amine groups (N2), being the unique component in (5/1/5) and (5/1/5)M, whereas (5/0/5) and (5/1/5)A also contain graphitic N (Fig. S5b). (5/1/5)A and (5/1/5)U are the only samples containing, respectively, pyridinic NO_x (14% of the deconvoluted area) and pyridinic N (37%) functionalization. It is important to note that the pyridinic and pyrrolic N groups are associated with vacancies in the graphene backbone, which could explain the presence of the observed nanometre-sized holes in the NrGO structure of the deposited samples (Fig. 2). The incorporation of nitrogen into the carbon structure could be either produced through (i) the direct chemical reaction of the GO-MWCNT functional groups with the precursor molecules and N_2

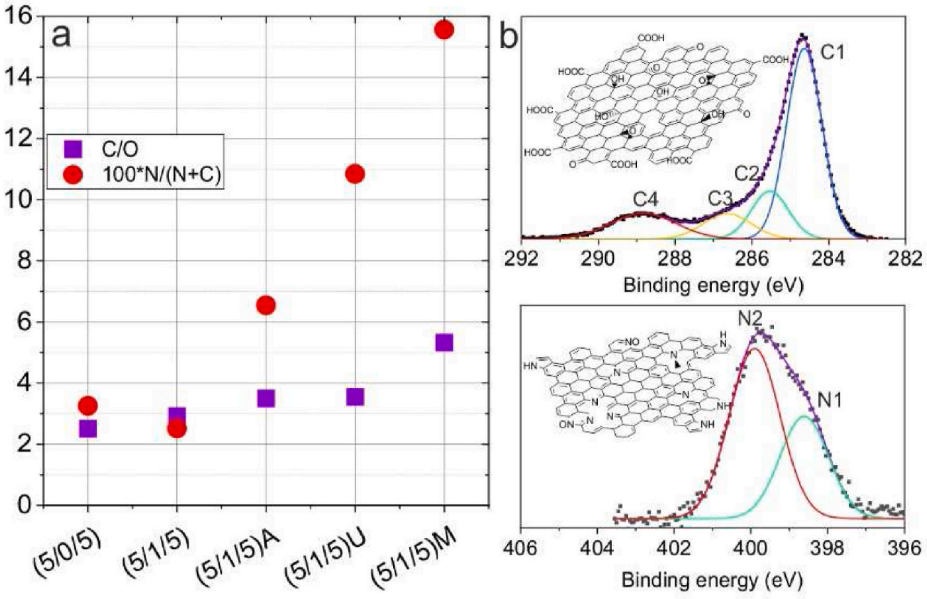

Fig. 3. (a) Relative elemental ratios calculated from XPS surveys. (b) C1s and N1s high resolution XPS spectra of (5/1/5)U. Insets: sketches of the envisaged rGO structure with oxygen and nitrogen containing groups.

ambient gas in the irradiation chamber, or (ii) the formation of a carbon nitride material by means of the thermal decomposition of the N-containing molecules, acting as an intermediate precursor for the formation of identified N-functional groups [14,50–54]. High resolution oxygen and nickel signals were also recorded. Representative O1s and Ni2p spectra are shown in Fig. S5c. O1s lines were deconvoluted into three components: O1 (centred at 529.7 eV), associated to double C=O bonds of carbonyl and carboxyl groups present in the rGO and MWCNT, besides Ni–O bonds of the NiO nanostructures; O2 (at 531.7 eV), which can be ascribed to defective sites and/or adsorbed oxygen in NiO crystals, as well as nickel hydroxide compounds; and O3 (at 533.2 eV), related to single C–O bonds of the hydroxyl and epoxy groups contained in the nanocarbons [55,56]. All the samples show similar configuration of the O1s components, being O1 the most intense peak. Finally, the spectra of the Ni2p doublet were deconvoluted into four components: Ni1 (at 856.1 eV) and Ni3 (at 873.8 eV) corresponding to $Ni2p_{3/2}$ and $Ni2p_{1/2}$ lines, respectively, and their associated shake-up satellites Ni2 (at 861.7 eV) and Ni4 (at 879.8 eV). Additionally, the (5/1/5)A sample exhibits the presence of a weak component centred at 853.8 eV. The position of these characteristic peaks point to the formation of NiO and $Ni(OH)_2$, formed by the chemical interaction of NiO molten droplets with evaporated H_2O molecules from the matrix [55,56].

Raman spectroscopy characterization was also carried out for the quantitative analysis of the laser-induced structural modification of the deposited carbon nanostructures. Several spectra were acquired at different sites of each deposited layer and were deconvoluted into five components centred at ca. 1190, 1360, 1490, 1600 and 1690 cm^{-1} referred to as I, D, D'', G and D' components, respectively (a typical deconvoluted spectrum is presented at the inset of Fig. 4a). The G band is generated by sp [2]-bonded carbons contained in the material, whereas the disorder-activated D band appears with the presence of defects in the graphitic structure (vacancies, boundaries, sp [3]-bonds) [57]. It is generally accepted the D/G intensity ratio (I_D/I_G) as a figure of merit for the study of the quantity of defects present in the graphene structure (the ratio of D/G integrated intensities can be also used). Thus, if the laser-generated defects destroy graphitic rings, I_D/I_G increases in a low-density defect regime (showing the opposite tendency in a high-density defect regime) [57–59]. Since the width of the G band always increases with the structural disorder, the I_D/I_G vs full width at the half maximum of G, FWHM (G), allow us to determine the defect regime of the rGO-MWCNT materials (Fig. 4a). As observed, the samples (5/1/5), (5/1/5)A, and (5/1/5)M reveal an increasing behaviour of I_D/I_G over FWHM (G) accounting for a regime of low density of defects. The samples (5/0/5) and (5/1/5)U exhibit the opposite tendency, pointing to the presence of a high density of structural defects. This study is worth to be carried out, since only attending the I_D/I_G values could erroneously induce us to affirm that the samples (5/0/5) and (5/1/5)U are the ones with the lowest density of defects (they show the lowest D/G intensity ratios, as shown in the inset of Fig. 4a). This is a very common mistake observed in the literature. According to the I_D/I_G vs FWHM (G) results, the mean distance between defects (L_D) and the corresponding density of defects (n_D) were calculated using the proper equations found elsewhere [57,59]. As observed in Fig. 4b, the samples (5/1/5), (5/1/5)A and (5/1/5)M disclose very similar values of L_D (ca. 12 nm) and n_D (ca. 2×10^{11} cm^{-2}), whereas (5/0/5) and (5/1/5)U reveal about one and two orders of magnitude lower L_D (ca. 1 nm) and higher n_D (ca. 2×10^{13} cm^{-2}), respectively.

D and D' are Raman-forbidden bands activated by the graphene's structural defects, and the characteristics of such bands depend on the type of defect [60]. Eckmann et al. demonstrated that the nature of the defects created in the deposited carbon nanostructures can be experimentally studied through the D/D' intensity ratio ($I_D/I_{D'}$) [61]. As witnessed in Fig. 4c, the (5/1/5), (5/1/5)A and (5/1/5)M samples, which contain lower density of defects, present a $I_D/I_{D'}$ ratio above 13 pointing to the main formation of sp [3]-bonded carbons. However, (5/0/5) and (5/1/5)U disclose a D/D' ratio of around 7.3 and 10.2, respectively,

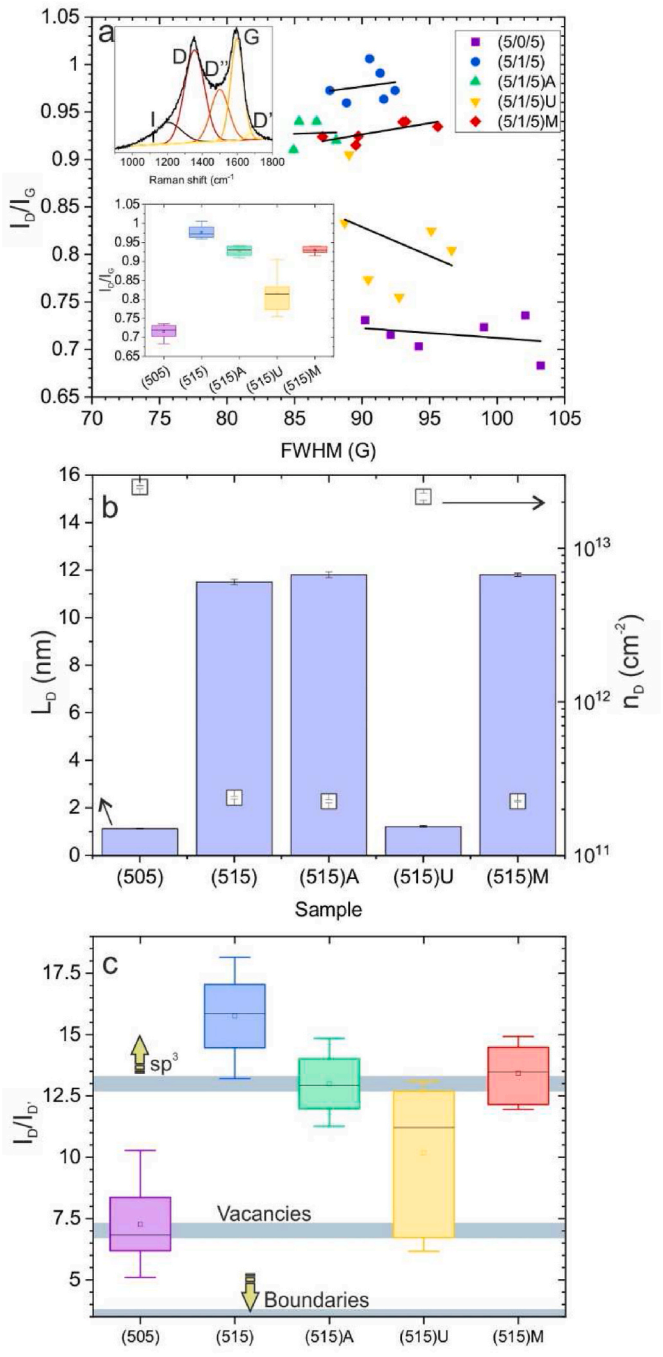

Fig. 4. D/G intensity ratio versus FWHM(G) of all the samples, including linear fits. Insets: deconvolution of a typical Raman spectrum and box plot of the measured D/G intensity ratios. (b) Calculated mean distance between defects (L_D) and corresponding density of defects (n_D). (c) Box plot of the D/D' intensity ratio for all the deposited samples.

suggesting the foremost creation of vacancies probably with some contribution of boundary-like defects. To summarize, the laser-induced deposition process prompts the formation of different densities and types of structural defects depending on the MAPLE target composition. Deposited composites constituted by NrGO and NiO NPs, (5/0/5), exhibit a high density of vacancy-like flaws in the NrGO structure due to the extreme thermal conditions experienced upon the UV laser irradiation process. The addition of MWCNTs (sample (5/1/5)) reveals two orders of magnitude lower density of sp [3]-like defects in the carbon structure. This result would point out to higher stability, i. e. lower

reactivity, of the MWCNTs as compared to the GO sheets during the UV-irradiation and subsequent thermal pulse – deposition, even though MWCNTs reach greater temperatures than GO sheets (Fig. 1). The sp [3]-bonding could be caused by the remaining carboxylic groups at the MWCNT structure as well as the amorphization processes detected by HRTEM. Notice that the reduction degree does not significantly increase according to XPS analyses, and pyrrolic N - amine groups are mainly created even in absence of MWCNTs (Fig. S5b) [23]. The interaction of GO sheets and MWCNTs with the precursor molecules leads to the formation of vacancies and boundaries at the graphitic network due to the incorporation of nitrogen groups. Remarkably, (5/1/5)U sample exhibits a much higher density of defects and the formation of vacancies/boundaries rather than sp [3]-C as compared to the other samples synthesized with N-containing precursors. This would account for higher reactivity and structural modifications of carbon nanostructures with urea molecules than with ammonia and melamine, probably due to the propensity of urea to interact through hydrogen bonds and π-π coupling with the GO-MWCNT functional groups and graphene domains [62–64].

For the determination of additional structural features at the nanoscale of the deposited composites, further characterization was carried out through GISAXS [65–67]. Fig. 5a presents the acquired intensity profiles as a function of the in-plane scattering vector (q) of all the samples. The scattered intensities at low q values follow the power law and scale with the scattering vector as $I(q) \propto 1/q^n$ [65,68,69]. The power law exponents were obtained by fitting the experimental data in the q-range below 0.24 nm^{-1} that corresponds to probing length scales ($d = 2\pi/q$) above 26 nm. The sample (5/0/5) is characterized by the highest exponent (2.14 ± 0.01). The incorporation of the MWCNTs to the samples results in the exponent decrease down to 1.42 ± 0.06 (averaged for all samples containing MWCNTs networks). Note that in our composite materials, the scattered intensity is a consequence of electron density fluctuations due to the presence of different types of nanomaterials (NrGO sheets, MWCNTs, NiO NPs) exhibiting a wealth of sizes, shapes, structural changes and pores. The proper modelling of the structure responses requires the measurements in larger q-range. Moreover, the q-range must cover at least one decade if the fractal dimension of the samples should be evaluated, i.e. USAXS/USANS measurements are required. Such study will be the subject of future work. Here, we rather focus on the qualitative description of accessibility to the pores in given q-range for nitrogen-containing samples which exhibit the presence of nm-sized holes as shown by TEM (Fig. 2b and c). We collected the GISAXS data during continuous up-down humidity ramps, which should show the partial filling of pores with water. In such a case the electron density variation should result in the form factor change and thus the scattered intensity. We split the q-range at 3.14 nm^{-1} (probing length scales below and above 2 nm) and calculate total integrated intensity, invariant, and correlation length in this ranges using the formalism taken from Ref. [70]. Fig. 5b depicts the correlation lengths as a very sensitive qualitative measure for changes of the scattering data in the corresponding ranges evaluated for (5/1/5)A and (5/1/5)U samples as function of time. The (5/1/5)A sample as well as (5/1/5)M one (data not shown) do not show any features while (5/1/5)U sample reversibly follows humidity ramp in both q-ranges suggesting that the surface chemistry is different within nitrogen-containing samples. It is worth recalling that the (5/1/5)U sample is the only one containing pyridinic N–C groups (Fig. S5b) and it has a high density of vacancies/boundaries as compared to the rest of the samples containing NrGO, NiO and MWCNTs (Fig. 4). At low q-range the correlation length of (5/1/5)U sample is decreasing with humidity increase suggesting that the volume fraction of pores is larger than the one of composite material. On the contrary, the correlation length increases at high q-range. These findings suggest that larger (>2 nm) pores prevail in (5/1/5)U sample but, more importantly, the reversible response in both q-ranges has been observed.

The electrochemical properties of the deposited samples, acting as electrodes in 1 M Na_2SO_4 aqueous electrolyte, were investigated through SPECS, scanning the applied voltage in steps of 25 mV in the 0–0.8 V range. After each voltage step, the measured current exhibited a peak-like evolution with time, as shown in Fig. S6a. The total current (i_{Tot}) was assumed to be the sum of capacitive (i_{Cap}), diffusional (i_{Diff}), and residual (i_{Res}) components ($i_{Tot} = i_{Cap} + i_{Diff} + i_{Res}$). The capacitive contribution is generated by the surface charge storage mechanisms (EDL and pseudocapacitance). The diffusional current is the result of slower diffusion-limited kinetic processes associated with intercalation, bulk insertion-de-insertion and redox reactions. The residual current accounts for the existence of incomplete redox reactions along the rest time between voltage steps that, indeed, could contribute to the self-discharge of the electrode. Therefore, all the current peaks were fitted using eqs. (1) and (2) for the capacitive and diffusional processes, being considered i_{Res} as a constant in time (Fig. S6b) [71–73].

$$i_{Cap} = \frac{\Delta V}{R_S} exp\left(-\frac{t}{R_S C_C}\right) \quad (1)$$

$$i_{Diff} = \frac{B}{\sqrt{t}} \quad (2)$$

In these equations, ΔV is the voltage step (25 mV), R_S is the series resistance of the electrode-electrolyte-cell system, C_C is the capacitance of the electrode, B is a parameter that depends on the diffusion coefficient, electrolyte concentration, number of electrons transferred in the redox reaction, as well as electrode's area (Cottrell equation); and t is the time after the voltage step. Fig. 6 presents the fitted values of C_C, R_S, B and i_{Res} as a function of the voltage step for all the deposited electrodes. Regardless of the dispersion and associated error of the fitted values, it can be stated that the (5/1/5)U electrode is the one with the highest capacitance in all the voltage range, closely followed by (5/1/5)A but statistically different. This fact has been verified by an ANOVA study of the capacitance calculated from multiple SPECS and cyclic voltammetry experiments (not shown). The (5/1/5) and (5/1/5)M electrodes exhibit

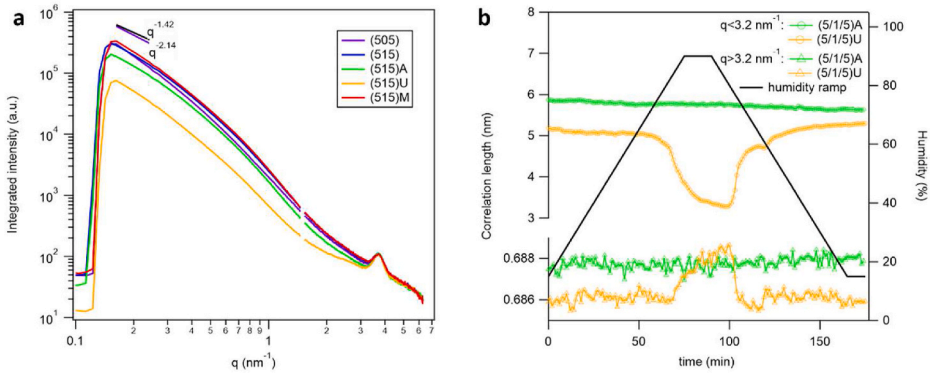

Fig. 5. (a) In-plane GISAXS intensity profiles of all the samples. The violet and black lines represent the fit range together with exponents obtained from power law for (505) sample (violet) and rest (averaged) of MWCNTs containing samples (black). The q-range below 0.16 nm^{-1} is the beamstop area. The origin of the peak at approx. 4 nm^{-1} is from kapton window. (b) Temporal evolution of correlation length at low (<3.2 nm^{-1}) and high (>3.2 nm^{-1}) q-ranges. The humidity ramp is depicted in black colour. (For interpretation of the references to colour in this figure legend, the reader is referred to the Web version of this article.)

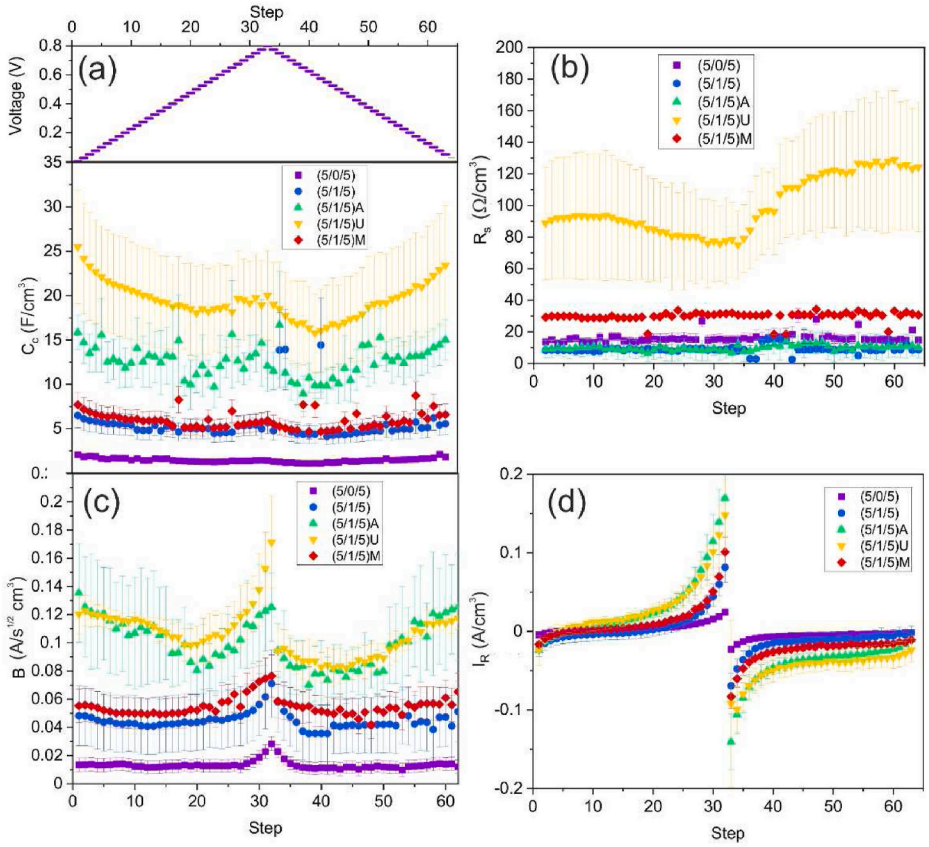

Fig. 6. Results obtained from fitting SPECS current peaks. (a) Voltage level and calculated C_c, (b) R_s, (c) B and (d) I_R parameters corresponding to each measurement step.

lower, and very similar, capacitance and (5/0/5) presents the lowest capacitance demonstrating that the addition of MWCNTs prompts an augment of the charge storage capability of the rGO-based composites [23]. Interestingly, (5/1/5)U also presents a significantly higher value of R_S as compared to the rest of the electrodes. Since the electrolyte, cell configuration and current collector are the same in all the experiments, the change of the series resistance should be attributed to chemical-structural modification of the active material of the electrode (already proved), perhaps with some interaction deviations at the interface between electrode and electrolyte (caused by surface redox reactions). The B parameters of the (5/1/5)U and (5/1/5)A electrodes are very similar and are higher than that of the rest of samples in all the voltage range. This fact would suggest higher values of either the effective area or the diffusion coefficient of (5/1/5)U and (5/1/5)A, considering an equal number of transferred electrons in their respective redox processes and similar ionic concentrations. The residual current increases with the applied voltage in a similar fashion in all the electrodes, being slightly higher in (5/1/5)U and (5/1/5)A.

From the SPECS data, it was possible to emulate cyclic voltammograms in the 4 × 10^{-4}-1.2 V/s sweep rate range [73]. As observed in Fig. 7a, the generated voltammograms present a rectangular-like shape pointing to surface processes (EDL and pseudocapacitive) as the main contribution to the stored charge. For a quantitative estimation, the measured current was considered to be the sum of the capacitive (i_{Cap}) and diffusional (i_{Diff}) components, neglecting the contribution of the residual current. The response current in an ideal capacitive regime shall be proportional to the sweep rate (s), whereas the diffusional current is proportional to $s^{1/2}$. Hence [74].

$$i_{Tot}(s,\ V) = i_{Cap} + i_{Diff} = k_1 s + k_2 s^{1/2} \quad (3)$$

k_1(V) and k_2(V) were determined by linear regression of $i_{Tot}/s^{1/2}$ vs $s^{1/2}$, and their substitution in eq. (3) allowed the evaluation of the contribution to the current of the capacitive (surface) processes and the diffusion-limited ones at each voltage (Fig. 7a). As expected, the percentage of the capacitive contribution, assessed by means of the ratio of the integrated current areas, increases with the sweep rate for all the electrodes due to the difficulties of diffusional ionic species to follow the fast voltage variations (Fig. 7b). At very slow rates, these diffusional processes are the prevalent ones. Interestingly, the (5/1/5)U electrode exhibits a significantly low capacitive contribution that could be interpreted as "battery-like" behaviour that disagrees with the results shown in Fig. 6. Nevertheless, the origin of this effect is connected to the fitting process. Fig. S7a shows two typical linear regressions of the total current versus the square root of the sweep rate. As observed, the data of the (5/1/5)A sample fits well in the full range, but the fade of the current at the highest sweep rates in (5/1/5)U causes a very poor fit. Certainly, a very low coefficient of determination is obtained in the full voltage range of (5/1/5)U (Fig. S7b), which is not observed in the other electrodes. This lack of linearity could be caused by the electric attenuation in the highly porous matrix of the electrode, exhibiting an additional augment of the resistance, which is not considered in eq. (3) [75,76]. Consequently, this "porous-electrode" effect also accounts for the significantly higher R_S values observed in (5/1/5)U as compared to the rest of the electrodes (Fig. 6b). Repeating the linear regression study of the (5/1/5)U sample but without considering the data related to the fastest sweep rates (s > 86.7 mV/s) allows obtaining fits with a coefficient of determination close to 1 in all the voltage range except at voltages close to 0.8 V. By doing so, the corresponding capacitive percentage increases considerably, becoming the highest one of all the set of samples (Fig. 7b). This result would be coherent with the higher C_C values of (5/1/5)U obtained from the current peaks regression study (Fig. 6a).

In most of the already published works, the enhancement of

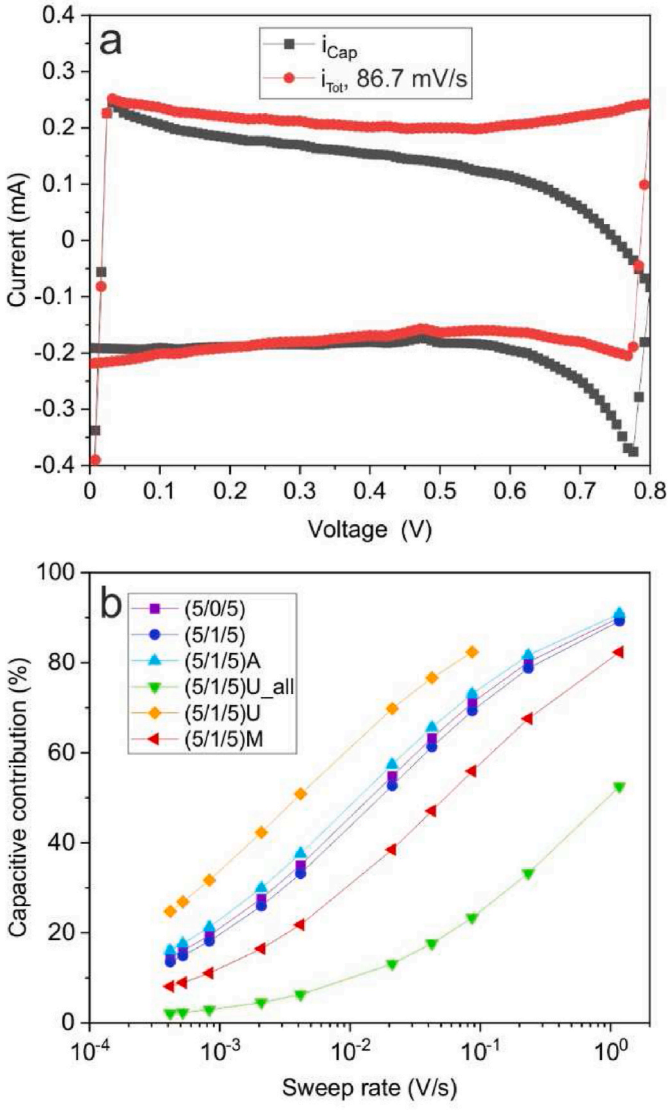

Fig. 7. (a) Typical cyclic voltammetry generated from SPECS data, corresponding to (5/1/5)U electrode at 86.7 mV/s sweep rate. The calculated current generated from the capacitive processes is also shown (i_{Cap}). (b) Percentage of the capacitive charge for all the electrodes. "(5/1/5)U_all" refers to the values calculated through linear regression considering all the sweep rate range, whereas "(5/1/5)U" denotes the assessment performed discarding the fastest sweep rates (higher than 86.7 mV/s).

capacitance observed in the N-doped graphene electrodes is mainly ascribed to different aspects related to the electric-faradaic behaviour of the N-containing functional groups and their influence in neighbouring carbon atoms [8,14,77–82]. Thereby, the graphitic N is considered to facilitate the electron transfer by triggering a decrease of the charge-transfer resistance of the n-type doped graphene. Pyridinic and pyrrolic N are also known for their activity in catalytic redox reactions, and pseudocapacitive nature is also attributed to them in charge-discharge processes (especially in pyridinic groups). Substitutional and pyridinic N also exhibit large dipole moments that would enhance the wettability of the electrode. Though the porosity is always present, much less amount of works "essentially" linked the increase of the charge storage performance to the nanomorphology resulting from the nitrogen-doping of graphene [28,29,83]. In our work, the results highlight the great influence of the structural configuration of the electrode at the nanoscale, in terms of crystalline defects, on the charge storage capacity. This structural effect, which is connected to the chemical functionalization, could be as important as the faradaic component. The kind of precursor molecule used for the N-doping process is a determining factor for achieving electrodes with one or other structural-electrochemical nature. The XPS, Raman spectroscopy, and GISAXS analyses revealed that the (5/1/5)U electrode, deposited through urea-mediated reactions, exhibits a much more porous structure than the rest of electrodes due to the presence of pyridinic N (associated with vacancies of carbon atoms and the presence of nanoholes [84]). This fact, probably in synergistic combination with the faradaic nature of the pyridinic N [85], would explain the observed great enhancement of the electrode's capacitance as compared to other electrodes with even more content of nitrogen and similar density of defects in the graphitic structure. An additional contribution could be also originated from the band structure modification of the graphene material due to the vacancies generated by the basal pyridinic N, and not by the nitrogen itself [86]. (5/1/5)A discloses about double capacitance than (5/1/5) and (5/1/5)M electrodes, probably due to the electric - faradaic action of the graphitic N and pyridinic N–O groups [16]. It has been also verified that the pyrrolic N groups, even being associated with structural holes, do not significantly contribute to the capacitance enhancement of our samples. It is worth noting that pyrrolic N groups have been previously considered to form at graphene basal plane and edges of plasma-fabricated N-doped graphene materials, whereas pyridinic N would preferentially form in the basal-plane [13]. Assuming this fact in our fabricated composites, edge pyrrolic N would not significantly influence the nanohole formation of the materials, to the contrary of basal pyridinic N groups (mostly contributing to EDL capacitance). Anyhow, the dynamics of ionic arrangement at nanopores comprehend complex mechanisms [87–89], and this hypothesis should be checked by means of advanced analyses of the structural configuration, for instance, through aberration-corrected HRTEM, *in operando* GISAXS and molecular dynamics (MD) - density functional theory (DFT) simulations.

4. Conclusion

The reactive inverse matrix assisted pulsed laser evaporation technique allows fabricating complex composite electrodes constituted by conductive N-doped rGO and MWCNTs functionalized with different nitrogen containing groups and decorated with NiO nanostructures. The high temperatures induced by the laser pulses in the carbon - NiO nanoentities besides the matrix surrounding them, trigger complex chemical reactions leading to phase transformations and heteroatom functionalization simultaneously to the deposition process. The introduction of the MWCNTs leads to an increase of the mesoporosity, providing enhanced diffusion paths for the electrolyte ionic species that prompts an increase in capacitance. Moreover, the nature of the N-containing precursor molecule generates remarkable differences in the constitution of the carbon nanoentities. Noteworthy, the electrode synthesized with urea precursor exhibits higher porosity and density of structural defects, of the vacancy-boundary types, than the analogue electrodes containing NrGO-MWCNTs-NiO. The difference of structural configuration at the nanoscale is likely to be correlated to the presence of pyridinic N groups, and leads to a significant increase of the capacitance of the electrode.

Declaration of competing interest

The authors declare that they have no known competing financial interests or personal relationships that could have appeared to influence the work reported in this paper.

Acknowledgement

The authors are grateful for the financial support of MCIN/AEI/10.13039/501100011033 under the project PID2020-116612RB-C31 and support from AGAUR of Generalitat de Catalunya through

projects 2017 SGR 1086 and 2017 SGR 1771. ICMAB acknowledges financial support from MCIN/AEI/10.13039/501100011033, through Severo Ochoa FUNFUTURE grant (CEX2019-000917-S). This project also received funding from the EU-H2020 research and innovation programme under the grant agreement No 654360 having benefited from the access provided by the Graz University of Technology and the Consiglio Nazionale delle Ricerche– Istituto Officina dei Materiali in Elettra-Sincrotrone Trieste (SAXS), and TEM and Raman spectroscopy installations, respectively, within the framework of the NFFA-Europe Transnational Access Activity (project ID 912). P.G.L thanks the financial support of the Spanish Ministry of Economy, Industry and Competitiveness through the grant BES-2017-081652 for the formation of scientific researchers. PR acknowledges the receipt of a fellowship from the ICTP Programme for Training and Research in Italian Laboratories, Trieste, Italy. The authors acknowledge Marco Lazzarino for acquiring the Raman spectra within the NFFA collaboration, as well as support of the publication fee by the CSIC Open Access Publication Support Initiative through its Unit of Information Resources for Research (URICI).

Appendix A. Supplementary data

Supplementary data to this article can be found online at https://doi.org/10.1016/j.ceramint.2022.02.128.

References

[1] A. Muzaffar, M.B. Ahamed, K. Deshmukh, J. Thirumalai, A Review on Recent Advances in Hybrid Supercapacitors: Design, Fabrication and Applications, Renewable and Sustainable Energy Reviews, 2019, pp. 123–145, https://doi.org/10.1016/j.rser.2018.10.026.

[2] Y.W. Chi, C.C. Hu, H.H. Shen, K.P. Huang, New approach for high-voltage electrical double-layer capacitors using vertical graphene nanowalls with and without nitrogen doping, Nano Lett. 16 (9) (2016) 5719–5727, https://doi.org/10.1021/acs.nanolett.6b02401.

[3] J. Liu, J. Wang, C. Xu, H. Jiang, C. Li, L. Zhang, J. Lin, Z.X. Shen, Advanced energy storage devices: basic principles, analytical methods, and rational materials design, Advanced Science. Wiley-VCH Verlag January 1 (2018) 1700322, https://doi.org/10.1002/advs.201700322.

[4] E. Pomerantseva, F. Bonaccorso, X. Feng, Y. Cui, Y. Gogotsi, Energy storage: the future enabled by nanomaterials, Science (2019) 969, https://doi.org/10.1126/science.aan8285.

[5] L. Hao, X. Li, L. Zhi, Carbonaceous electrode materials for supercapacitors, Adv. Mater. (2013), https://doi.org/10.1002/adma.201301204.

[6] S. Wang, Z.S. Wu, S. Zheng, F. Zhou, C. Sun, H.M. Cheng, X. Bao, Scalable fabrication of photochemically reduced graphene-based monolithic micro-supercapacitors with superior energy and power densities, ACS Nano (2017), https://doi.org/10.1021/acsnano.7b01390.

[7] R. Raccichini, A. Varzi, S. Passerini, B. Scrosati, The role of graphene for electrochemical energy storage, Nat. Mater. 14 (3) (2015) 271–279, https://doi.org/10.1038/nmat4170.

[8] X. Wang, G. Sun, P. Routh, D.H. Kim, W. Huang, P. Chen, Heteroatom-doped graphene materials: syntheses, properties and applications, Chem. Soc. Rev. Royal Soc. Chem. October 21 (2014) 7067–7098, https://doi.org/10.1039/c4cs00141a.

[9] S.T. Pantelides, Y. Puzyrev, L. Tsetseris, B. Wang, Defects and doping and their role in functionalizing graphene, MRS Bull. 37 (12) (2012) 1187–1194, https://doi.org/10.1557/mrs.2012.187.

[10] F. Bonaccorso, L. Colombo, G. Yu, M. Stoller, V. Tozzini, A.C. Ferrari, R.S. Ruoff, V. Pellegrini, Graphene, related two-dimensional crystals, and hybrid systems for energy conversion and storage, Sci. Am. Assoc. Adv. Sci. January 2 (2015), https://doi.org/10.1126/science.1246501.

[11] E.E. Miller, Y. Hua, F.H. Tezel, Materials for energy storage: review of electrode materials and methods of increasing capacitance for supercapacitors, J. Energy Storage (2018) 30–40, https://doi.org/10.1016/j.est.2018.08.009.

[12] C.H.A. Tsang, H. Huang, J. Xuan, H. Wang, D.Y.C. Leung, Graphene Materials in Green Energy Applications: Recent Development and Future Perspective, Renewable and Sustainable Energy Reviews, 2020, p. 109656, https://doi.org/10.1016/j.rser.2019.109656.

[13] H.M. Jeong, J.W. Lee, W.H. Shin, Y.J. Choi, H.J. Shin, J.K. Kang, J.W. Choi, Nitrogen-doped graphene for high-performance ultracapacitors and the importance of nitrogen-doped sites at basal planes, Nano Lett. 11 (6) (2011) 2472–2477, https://doi.org/10.1021/nl2009058.

[14] H.L. Guo, P. Su, X. Kang, S.K. Ning, Synthesis and characterization of nitrogen-doped graphene hydrogels by hydrothermal route with urea as reducing-doping agents, J. Mater. Chem. 1 (6) (2013) 2248–2255, https://doi.org/10.1039/c2ta00887d.

[15] C.T. Hsieh, H. Teng, Influence of oxygen treatment on electric double-layer capacitance of activated carbon fabrics, Carbon N. Y. 40 (5) (2002) 667–674, https://doi.org/10.1016/S0008-6223(01)00182-8.

[16] D. Hulicova-Jurcakova, M. Seredych, G.Q. Lu, T.J. Bandosz, Combined effect of nitrogen- and oxygen-containing functional groups of microporous activated carbon on its electrochemical performance in supercapacitors, Adv. Funct. Mater. (2009), https://doi.org/10.1002/adfm.200801236.

[17] J. Li, L. Lin, D. Rui, Q. Li, J. Zhang, N. Kang, Y. Zhang, H. Peng, Z. Liu, H.Q. Xu, Electron-hole symmetry breaking in charge transport in nitrogen-doped graphene, ACS Nano 11 (5) (2017) 4641–4650, https://doi.org/10.1021/acsnano.7b00313.

[18] Y. Esqueda-Barrón, A. Pérez del Pino, P.G. Lebière, A. Musheghyan-Avetisyan, E. Bertran-Serra, E. György, C. Logofatu, Boost of charge storage performance of graphene nanowall electrodes by laser-induced crystallization of metal oxide nanostructures, ACS Appl. Mater. Interfaces 13 (15) (2021) 17957–17970, https://doi.org/10.1021/acsami.1c00951.

[19] N. Choudhary, C. Li, J. Moore, N. Nagaiah, L. Zhai, Y. Jung, J. Thomas, Asymmetric supercapacitor electrodes and devices, Adv. Mater. 29 (21) (2017) 1605336, https://doi.org/10.1002/adma.201605336.

[20] Y. Bai, M. Du, J. Chang, J. Sun, L. Gao, Supercapacitors with high capacitance based on reduced graphene oxide/carbon nanotubes/NiO composite electrodes, J. Mater. Chem. 2 (11) (2014) 3834–3840, https://doi.org/10.1039/c3ta15004f.

[21] Á. Pérez Del Pino, A. Martínez Villarroya, A. Chuquitarqui, C. Logofatu, D. Tonti, E. György, Reactive laser synthesis of nitrogen-doped hybrid graphene-based electrodes for energy storage, J. Mater. Chem. 6 (33) (2018) 16074–16086, https://doi.org/10.1039/c8ta03830a.

[22] R. Kumar, S. Sahoo, E. Joanni, R.K.R.K. Singh, R.M.R.M. Yadav, R.K.R.K. Verma, D. P.D.P. Singh, W.K.W.K. Tan, A. Pérez del Pino, S.A. Moshkalev, A. Matsuda, A Review on Synthesis of Graphene, H-BN and MoS2 for Energy Storage Applications: Recent Progress and Perspectives, 12, 2019, pp. 2655–2694, https://doi.org/10.1007/s12274-019-2467-8.

[23] Á. Pérez Del Pino, M. Rodríguez López, M.A. Ramadan, P. García Lebière, C. Logofatu, I. Martínez-Rovira, I. Yousef, E. György, Enhancement of the supercapacitive properties of laser deposited graphene-based electrodes through carbon nanotube loading and nitrogen doping, Phys. Chem. Chem. Phys. 21 (45) (2019) 25175–25186, https://doi.org/10.1039/c9cp04237g.

[24] R. Ivan, C. Popescu, A. Pérez del Pino, C. Logofatu, E. György, Carbon-based nanomaterials and ZnO ternary compound layers grown by laser technique for environmental and energy storage applications, Appl. Surf. Sci. 509 (2020), https://doi.org/10.1016/j.apsusc.2020.145359.

[25] A. Queraltó, E. György, R. Ivan, Á.P. Del Pino, R. Frohnhoven, S. Mathur, Enhanced UV-Vis photodegradation of nanocomposite reduced graphene oxide/ferrite nanofiber films prepared by laser-assisted evaporation, Crystals (2020), https://doi.org/10.3390/cryst10040271.

[26] P. García Lebière, Á. Pérez Del Pino, G.D. Domingo, C. Logofatu, I. Martínez-Rovira, I. Yousef, E. György, Laser fabrication of hybrid electrodes composed of nanocarbons mixed with cerium and manganese oxides for supercapacitive energy storage, J. Mater. Chem. 9 (2) (2021) 1192–1206, https://doi.org/10.1039/d0ta06756c.

[27] Á. Pérez del Pino, M.A. Ramadan, P. Garcia Lebière, R. Ivan, C. Logofatu, I. Yousef, E. György, Fabrication of graphene-based electrochemical capacitors through reactive inverse matrix assisted pulsed laser evaporation, Appl. Surf. Sci. 484 (2019) 245–256, https://doi.org/10.1016/j.apsusc.2019.04.127.

[28] X. Wu, J. Zhou, W. Xing, Y. Zhang, P. Bai, B. Xu, S. Zhuo, Q. Xue, Z. Yan, Insight into high areal capacitances of low apparent surface area carbons derived from nitrogen-rich polymers, Carbon N. Y. 94 (2015) 560–567, https://doi.org/10.1016/j.carbon.2015.07.038.

[29] W. Yuan, Y. Zhou, Y. Li, C. Li, H. Peng, J. Zhang, Z. Liu, L. Dai, G. Shi, The edge- and basal-plane-specific Electrochemistry of a single-layer graphene sheet, Sci. Rep. 3 (2013) 2248, https://doi.org/10.1038/srep02248.

[30] S.M. Omalley, J. Tomko, A.P.D. Pino, C. Logofatu, E. György, Resonant infrared and ultraviolet matrix-assisted pulsed laser evaporation of titanium oxide/graphene oxide composites: a comparative study, J. Phys. Chem. C 118 (48) (2014), https://doi.org/10.1021/jp509067u.

[31] A. Pérez del Pino, E. Gyorgy, S. Hussain, J.L. Andújar, E. Pascual, R. Amade, E. Bertrán, Laser-induced nanostructuration of vertically aligned carbon nanotubes coated with nickel oxide nanoparticles, J. Mater. Sci. 52 (7) (2017) 4002–4015, https://doi.org/10.1007/s10853-016-0662-5.

[32] Á.P.D. Pino, E. György, C. Logofatu, A. Duta, Study of the deposition of graphene oxide by matrix-assisted pulsed laser evaporation, J. Phys. D Appl. Phys. 46 (50) (2013), https://doi.org/10.1088/0022-3727/46/50/505309.

[33] Á. Pérez Del Pino, E. György, L. Cabana, B. Ballesteros, G. Tobias, Ultraviolet pulsed laser irradiation of multi-walled carbon nanotubes in nitrogen atmosphere, J. Appl. Phys. 115 (9) (2014), https://doi.org/10.1063/1.4864776.

[34] H. Amenitsch, M. Rappolt, M. Kriechbaum, H. Mio, P. Laggner, S. Bernstorff, IUCr, First performance assessment of the small-angle X-ray scattering beamline at ELETTRA, urn:issn:0909-0495 5, 1998, pp. 506–508, https://doi.org/10.1107/S090904959800137X, 3.

[35] M. Burian, C. Meisenbichler, D. Naumenko, H. Amenitsch, SAXSDOG: Open Software for Real-Time Azimuthal Integration of 2D Scattering Images, 2020.

[36] E. György, A. Prez Del Pino, G. Sauthier, A. Figueras, Biomolecular papain thin films grown by matrix assisted and conventional pulsed laser deposition: a comparative study, J. Appl. Phys. 106 (11) (2009), https://doi.org/10.1063/1.3266670.

[37] D. Hessen, UV Radiation and Arctic Ecosystems, Springer, Berlin, 2002.

[38] I.M. Klotz, T. Askounis, Absorption spectra and tautomerism of cyanuric acid, melamine and some related compounds, J. Am. Chem. Soc. 69 (4) (1947) 801–803, https://doi.org/10.1021/ja01196a017.

[39] J. Rima, M. Abourida, T. Xu, I.K. Cho, S. Kyriacos, New spectrophotometric method for the quantitative determination of melamine using mannich reaction, J. Food Compos. Anal. 22 (7–8) (2009) 689–693, https://doi.org/10.1016/j.jfca.2009.02.010.

[40] V.A. Smirnov, A.A. Arbuzov, Y.M. Shul'ga, S.A. Baskakov, V.M. Martynenko, V. E. Muradyan, E.I. Kresova, Photoreduction of graphite oxide, High Energy Chem. (2011), https://doi.org/10.1134/S0018143911010176.

[41] Z. Wan, E.W. Streed, M. Lobino, S. Wang, R.T. Sang, I.S. Cole, D.V. Thiel, Q. Li, Laser-reduced graphene: synthesis, properties, and applications, Adv. Mater. Technol. (2018), https://doi.org/10.1002/admt.201700315.

[42] Á. Pérez Del Pino, E. György, L. Cabana, B. Ballesteros, G. Tobias, Deposition of functionalized single wall carbon nanotubes through matrix assisted pulsed laser evaporation, Carbon N. Y. 50 (12) (2012), https://doi.org/10.1016/j.carbon.2012.05.023.

[43] N.R. Wilson, P.A. Pandey, R. Beanland, R.J. Young, I.A. Kinloch, L. Gong, Z. Liu, K. Suenaga, J.P. Rourke, S.J. York, J. Sloan, Graphene oxide: structural analysis and application as a highly transparent support for electron microscopy, ACS Nano 3 (9) (2009) 2547–2556, https://doi.org/10.1021/nn900694t.

[44] A. Ganguly, S. Sharma, P. Papakonstantinou, J. Hamilton, Probing the thermal deoxygenation of graphene oxide using high-resolution in situ X-ray-based spectroscopies, J. Phys. Chem. C (2011), https://doi.org/10.1021/jp203741y.

[45] A. Pérez Del Pino, E. György, C. Logofatu, J. Puigmartí-Luis, W. Gao, Laser-induced chemical transformation of graphene oxide-iron oxide nanoparticles composites deposited on polymer substrates, Carbon N. Y. 93 (2015) 373–383, https://doi.org/10.1016/j.carbon.2015.05.078.

[46] A. Queraltó, Á. Pérez del Pino, C. Logofatu, A. Datcu, R. Amade, I. Alshaikh, E. Bertran, I. Urzica, E. György, MAPLE synthesis of reduced graphene oxide/silver nanocomposite electrodes: influence of target composition and gas ambience, J. Alloys Compd. 726 (2017), https://doi.org/10.1016/j.jallcom.2017.08.052.

[47] A. Queraltó, A.P. del Pino, C. Logofatu, A. Datcu, R. Amade, E. Bertran-Serra, E. György, Reduced graphene oxide/Iron oxide nanohybrid flexible electrodes grown by laser-based technique for energy storage applications, Ceram. Int. 44 (16) (2018) 20409–20416, https://doi.org/10.1016/j.ceramint.2018.08.034.

[48] S. Sandoval, N. Kumar, J. Oro-Solé, A. Sundaresan, C.N.R. Rao, A. Fuertes, G. Tobias, Tuning the nature of nitrogen atoms in N-containing reduced graphene oxide, Carbon N. Y. 96 (2016) 594–602, https://doi.org/10.1016/j.carbon.2015.09.085.

[49] Z. Lin, G. Waller, Y. Liu, M. Liu, C.P. Wong, Facile synthesis of nitrogen-doped graphene via pyrolysis of graphene oxide and urea, and its electrocatalytic activity toward the oxygen-reduction reaction, Adv. Energy Mater. 2 (7) (2012) 884–888, https://doi.org/10.1002/aenm.201200038.

[50] Z. Wang, P. Li, Y. Chen, J. Liu, H. Tian, J. Zhou, W. Zhang, Y. Li, Synthesis of nitrogen-doped graphene by chemical vapour deposition using melamine as the sole solid source of carbon and nitrogen, J. Mater. Chem. C 2 (35) (2014) 7396–7401, https://doi.org/10.1039/c4tc00924j.

[51] T.F. Yeh, S.J. Chen, C.S. Yeh, H. Teng, Tuning the electronic structure of graphite oxide through ammonia treatment for photocatalytic generation of H2 and O2 from water splitting, J. Phys. Chem. C (2013), https://doi.org/10.1021/jp312613r.

[52] A. Gomathi, S. Reshma, C.N.R. Rao, A simple urea-based route to ternary metal oxynitride nanoparticles, J. Solid State Chem. 182 (1) (2009) 72–76, https://doi.org/10.1016/j.jssc.2008.10.004.

[53] D.R. Dreyer, S. Park, C.W. Bielawski, R.S. Ruoff, The Chemistry of Graphene Oxide, Chemical Society Reviews, 2010, pp. 228–240, https://doi.org/10.1039/b917103g.

[54] Z. Lin, M.K. Song, Y. Ding, Y. Liu, M. Liu, C.P. Wong, Facile preparation of nitrogen-doped graphene as a metal-free catalyst for oxygen reduction reaction, Phys. Chem. Chem. Phys. 14 (10) (2012) 3381–3387, https://doi.org/10.1039/c2cp00032f.

[55] P. García Lebière, A. Pérez del Pino, C. Logofatu, E. György, Laser synthesis of NixZnyO/reduced graphene oxide/carbon nanotube electrodes for energy storage applications, Appl. Surf. Sci. 563 (2021) 150234, https://doi.org/10.1016/J.APSUSC.2021.150234.

[56] M.C. Biesinger, B.P. Payne, L.W.M. Lau, A. Gerson, R.S.C. Smart, X-ray photoelectron spectroscopic chemical state quantification of mixed nickel metal, oxide and hydroxide systems, Surf. Interface Anal. 41 (4) (2009) 324–332, https://doi.org/10.1002/SIA.3026.

[57] A.C. Ferrari, D.M. Basko, Raman spectroscopy as a versatile tool for studying the properties of graphene, Nat. Nanotechnol. (2013) 235–246, https://doi.org/10.1038/nnano.2013.46.

[58] L.G. Cançado, M.G. Da Silva, E.H. Martins Ferreira, F. Hof, K. Kampioti, K. Huang, A. Pénicaud, C.A. Achete, R.B. Capaz, A. Jorio, Disentangling contributions of point and line defects in the Raman spectra of graphene-related materials, 2D Mater. 4 (2) (2017), 025039, https://doi.org/10.1088/2053-1583/aa5e77.

[59] L.G. Cançado, A. Jorio, E.H.M. Ferreira, F. Stavale, C.A. Achete, R.B. Capaz, M.V. O. Moutinho, A. Lombardo, T.S. Kulmala, A.C. Ferrari, Quantifying defects in graphene via Raman spectroscopy at different excitation energies, Nano Lett. 11 (8) (2011) 3190–3196, https://doi.org/10.1021/nl201432g.

[60] P. Venezuela, M. Lazzeri, F. Mauri, Theory of double-resonant Raman spectra in graphene: intensity and line shape of defect-induced and two-phonon bands, Phys. Rev. B Condens. Matter 84 (3) (2011), 035433, https://doi.org/10.1103/PHYSREVB.84.035433/FIGURES/29/MEDIUM.

[61] A. Eckmann, A. Felten, A. Mishchenko, L. Britnell, R. Krupke, K.S. Novoselov, C. Casiraghi, Probing the nature of defects in graphene by Raman spectroscopy, Nano Lett. 12 (8) (2012) 3925–3930, https://doi.org/10.1021/nl300901a.

[62] E.M. Schön, E. Marqués-Lõpez, R.P. Herrera, C. Alemán, D.D. Díaz, Exploiting molecular self-assembly: from urea-based organocatalysts to multifunctional supramolecular gels, Chem. Eur J. 20 (34) (2014) 10720–10731, https://doi.org/10.1002/chem.201402436.

[63] J.G. Hardy, R.C. Cornelison, R.C. Sukhavasi, R.J. Saballos, P. Vu, D.L. Kaplan, C. E. Schmidt, Electroactive tissue scaffolds with aligned pores as instructive platforms for biomimetic tissue engineering, Bioengineering 2 (1) (2015) 15–34, https://doi.org/10.3390/bioengineering2010015.

[64] W.J. Ong, L.L. Tan, S.P. Chai, S.T. Yong, Graphene oxide as a structure-directing agent for the two-dimensional interface engineering of sandwich-like graphene-g-C3N4 hybrid nanostructures with enhanced visible-light photoreduction of CO2 to methane, Chem. Commun. 51 (5) (2015) 858–861, https://doi.org/10.1039/c4cc08996k.

[65] T. Li, A.J. Senesi, B. Lee, Small angle X-ray scattering for nanoparticle research, Chem. Rev. Am. Chem. Soc. September 28 (2016) 11128–11180, https://doi.org/10.1021/acs.chemrev.5b00690.

[66] A. Hexemer, P. Müller-Buschbaum, Advanced grazing-incidence techniques for modern soft-matter materials analysis, urn:issn:2052-2525 2, 2015, pp. 106–125, https://doi.org/10.1107/S2052252514024178, 1.

[67] J. Liu, K.G. Yager, Unwarping GISAXS Data. *urn:issn:2052-2525* 5 (6) (2018) 737–752, https://doi.org/10.1107/S2052252518012058.

[68] J. Teixeira, IUCr. Small-angle scattering by fractal systems, urn:issn:*0021-8898* 21 (6) (1988) 781–785, https://doi.org/10.1107/S0021889888000263.

[69] M.P. Weir, D.W. Johnson, S.C. Boothroyd, R.C. Savage, R.L. Thompson, S. R. Parnell, A.J. Parnell, S.M. King, S.E. Rogers, K.S. Coleman, N. Clarke, Extrinsic wrinkling and single exfoliated sheets of graphene oxide in polymer composites, Chem. Mater. 28 (6) (2016) 1698–1704, https://doi.org/10.1021/ACS.CHEMMATER.5B04502.

[70] O. Glatter, Scattering methods and their application in colloid and interface science, Scatt. Methods their Appl. Colloid Interface Sci. (2018) 1–404, https://doi.org/10.1016/C2016-0-04640-5.

[71] M. Forghani, S.W. Donne, Method comparison for deconvoluting capacitive and pseudo-capacitive contributions to electrochemical capacitor electrode behavior, J. Electrochem. Soc. 165 (3) (2018) A664–A673, https://doi.org/10.1149/2.0931803jes.

[72] A.J. Gibson, S.W. Donne, A step potential electrochemical spectroscopy (SPECS) investigation of anodically electrodeposited thin films of manganese dioxide, J. Power Sources 359 (2017) 520–528, https://doi.org/10.1016/j.jpowsour.2017.05.082.

[73] M.F. Dupont, S.W. Donne, A step potential electrochemical spectroscopy analysis of electrochemical capacitor electrode performance, Electrochim. Acta 167 (2015) 268–277, https://doi.org/10.1016/j.electacta.2015.03.137.

[74] V. Augustyn, P. Simon, B. Dunn, Pseudocapacitive oxide materials for high-rate electrochemical energy storage, Energy Environ. Sci. (2014) 1597–1614, https://doi.org/10.1039/c3ee44164d.

[75] T.-C. Liu, W.G. Pell, B.E. Conway, S.L. Roberson, Behavior of molybdenum nitrides as materials for electrochemical capacitors: comparison with ruthenium oxide, J. Electrochem. Soc. 145 (6) (1998) 1882, https://doi.org/10.1149/1.1838571.

[76] E. Barsoukov, R.M. J (Eds.), Impedance Spectroscopy: Theory, Experiment, and Applications, third ed., John Wiley & Sons, Inc., 2018 https://doi.org/10.1002/9781119381860.

[77] K. Akada, T. Terasawa, G. Imamura, S. Obata, K. Saiki, Control of work function of graphene by plasma assisted nitrogen doping, Appl. Phys. Lett. 104 (13) (2014) 131602, https://doi.org/10.1063/1.4870424.

[78] H. Wang, T. Maiyalagan, X. Wang, Review on recent progress in nitrogen-doped graphene: synthesis, characterization, and its potential applications, ACS Catal. 2 (5) (2012) 781–794, https://doi.org/10.1021/CS200652Y.

[79] Z. Luo, S. Lim, Z. Tian, J. Shang, L. Lai, B. MacDonald, C. Fu, Z. Shen, T. Yu, J. Lin, Pyridinic N doped graphene: synthesis, electronic structure, and electrocatalytic property, J. Mater. Chem. 21 (22) (2011) 8038–8044, https://doi.org/10.1039/C1JM10845J.

[80] D. Guo, R. Shibuya, C. Akiba, S. Saji, T. Kondo, J. Nakamura, Active sites of nitrogen-doped carbon materials for oxygen reduction reaction clarified using model catalysts, Science (80-.) 351 (6271) (2016) 361–365, https://doi.org/10.1126/SCIENCE.AAD0832.

[81] Z.-H. Sheng, L. Shao, J.-J. Chen, W.-J. Bao, F.-B. Wang, X.-H. Xia, Catalyst-free synthesis of nitrogen-doped graphene via thermal annealing graphite oxide with melamine and its excellent electrocatalysis, ACS Nano 5 (6) (2011) 4350–4358, https://doi.org/10.1021/NN103584T.

[82] A. Śliwak, B. Grzyb, N. Díez, G. Gryglewicz, Nitrogen-doped reduced graphene oxide as electrode material for high rate supercapacitors, Appl. Surf. Sci. 399 (2017) 265–271, https://doi.org/10.1016/J.APSUSC.2016.12.060.

[83] F. Zheng, Y. Yang, Q. Chen, High lithium anodic performance of highly nitrogen-doped porous carbon prepared from a metal-organic framework, Nat. Commun. *2014 51* 5 (1) (2014) 1–10, https://doi.org/10.1038/ncomms6261.

[84] Y.-C. Lin, P.-Y. Teng, C.-H. Yeh, M. Koshino, P.-W. Chiu, K. Suenaga, Structural and chemical dynamics of pyridinic-nitrogen defects in graphene, Nano Lett. 15 (11) (2015) 7408–7413, https://doi.org/10.1021/ACS.NANOLETT.5B02831.

[85] N.D.K. Tu, S.O. Park, J. Park, Y. Kim, S.K. Kwak, S.J. Kang, Pyridinic-nitrogen-containing carbon cathode: efficient electrocatalyst for seawater batteries, ACS Appl. Energy Mater. 3 (2) (2020) 1602–1608, https://doi.org/10.1021/ACSAEM.9B02087.

[86] R.J. Koch, M. Weser, W. Zhao, F. Viñes, K. Gotterbarm, S.M. Kozlov, O. Höfert, M. Ostler, C. Papp, J. Gebhardt, H.-P. Steinrück, A. Görling, T. Seyller, Growth and electronic structure of nitrogen-doped graphene on Ni(111), Phys. Rev. B 86 (7) (2012), 075401, https://doi.org/10.1103/PhysRevB.86.075401.

[87] C. Prehal, C. Koczwara, H. Amenitsch, V. Presser, O. Paris, Salt concentration and charging velocity determine ion charge storage mechanism in nanoporous supercapacitors, Nat. Commun. *2018 91* 9 (1) (2018) 1–8, https://doi.org/10.1038/s41467-018-06612-4.

[88] C. Prehal, C. Koczwara, N. Jäckel, A. Schreiber, M. Burian, H. Amenitsch, M. A. Hartmann, V. Presser, O. Paris, Quantification of ion confinement and desolvation in nanoporous carbon supercapacitors with modelling and in situ X-ray scattering, Nat. Energy *2017 23* 2 (3) (2017) 1–8, https://doi.org/10.1038/nenergy.2016.215.

[89] C. Prehal, D. Weingarth, E. Perre, R.T. Lechner, H. Amenitsch, O. Paris, V. Presser, Tracking the structural arrangement of ions in carbon supercapacitor nanopores using in situ small-angle X-ray scattering, Energy Environ. Sci. 8 (6) (2015) 1725–1735, https://doi.org/10.1039/C5EE00488H.